Supporting information for:

Self-Assembled Metal Cluster/Perovskite Catalyst for Efficient Acidic Hydrogen Production with an Ultra-Low Overpotential of 62 mV and over 1500 Hours of Stability at 1 A cm^{-2}

Yalei Fan[1,2,8], Jianfa Zhao[3,8], Jing Zhou[4], Wei-Hsiang Huang[5], Jianqiu Zhu[1], Chang-Yang Kuo[5,6], Shengjie Zhang[1], Chih-Wen Pao[5], Ting-Shan Chan[5], Yuxuan Zhang[1], Su-Yang Hsu[5], Jin-Ming Chen[5], Chien-Te Chen[5], Changqing Jin[3], Liu Hao Tjeng[7], Jian-Qiang Wang[1,2]*, Zhiwei Hu[7]*, & Linjuan Zhang[1,2]*

1. Key Laboratory of Interfacial Physics and Technology, Shanghai Institute of Applied Physics, Chinese Academy of Sciences, Shanghai 201800, P. R. China.
2. University of Chinese Academy of Sciences, Beijing 100049, P. R. China.
3. Beijing National Laboratory for Condensed Matter Physics, Institute of Physics, Chinese Academy of Sciences, Beijing 100190, P. R. China.
4. Zhejiang Institute of Photoelectronics and Zhejiang Institute for Advanced Light Source, Zhejiang Normal University, Jinhua, Zhejiang 321004, P. R. China.
5. National Synchrotron Radiation Research Center, Hsinchu 300, Taiwan, R. O. China.
6. Department of Electrophysics, National Yang Ming Chiao Tung University, Hsinchu 300, Taiwan, R. O. China.
7. Max Planck Institute for Chemical Physics of Solids, Dresden 01187, Germany.
8. Y.F. and J.Z. contributed equally to this work.

E-mail: wangjianqiang@sinap.ac.cn (J.-Q. Wang)

E-mail: Zhiwei.hu@cpfs.mpg.de (Z. Hu)

E-mail: zhanglinjuan@sinap.ac.cn (L. Zhang)

Methods

Chemicals

The CaO (99.99%), RuO_2 (99.995%), Co_3O_4 (99.99%), and $KClO_4$ (99.9%) were purchased from Alfa. The H_2SO_4 (liquid, ≥ 99%) and isopropanol (C_3H_8O, liquid, ≥ 99.5%) were purchased from Sinopharm Chemical Reagent Co., Ltd. The 20% Pt/C, 20% Ir/C and 5 wt % Nafion solution were purchased from Aladdin. The WO_3 (99.9%), D_2SO_4 (99%) and D_2O (99%) were purchased from Adamas-beta. The carbon paper was purchased from Toray. The Ti felt was purchased from Sinero Technology. The Nafion 117 membrane (183 μm) was purchased from DuPont.

Catalyst synthesis

The CCRO double perovskites were successfully synthesized using the solid-phase method under high-pressure and high-temperature conditions. The starting materials CaO (Alfa, 99.99% pure), RuO_2, Co_3O_4, and $KClO_4$ were mixed homogenously in a molar ratio 2:1:1/3:1/2 and pressed into a pellet with diameter 6 mm and height 4 mm in an argon-filled glovebox. Then, the pre-pressed pellet was sealed in a gold capsule. Note that the role of $KClO_4$ is to create an oxygen atmosphere during the high-pressure synthesis. High-pressure experiments were performed using a cubic anvil-type high-pressure apparatus, which is similar to those used for synthesizing $CaCoO_3$ or $BiCoO_3$ as described elsewhere.[1,2] After the pressure was gradually increased to 5 GPa, the sample was heated to 1050 °C within 5 min and maintained for 30 min. Then the temperature was quenched to room temperature prior to the slow release of pressure. The bulk CCRO sample was finely ground into powder and washed with deionized water several times in order to remove the residual KCl. Then, the CCRO powder was dried at 150°C for 1 h under air conditions. After the above process, the single-phase CCRO sample was obtained.

Structural characterization

The structure of the catalyst was determined by X-ray diffraction using a Bruker D8 Advance X-ray diffractometer with Cu Kα radiation (λ = 1.5418 Å). An FEI Tecnai G2 F20 S-TWIN electron microscope was used to conduct HRTEM. A Zeiss Crossbeam 540 was used to conduct SEM measurements. HAADF-STEM images were recorded via aberration-corrected FEI Themis Z STEM. For the FIB-TEM analysis: Firstly, the cutting position was determined using the SEM-FIB system.

Then, a platinum protective layer was applied to safeguard the surface area, followed by the formation of a thin foil through a stripping and thinning process. The thickness of the resulting thinned sheet is ~50 nm. Finally, TEM characterization of the thin sections was performed. The Raman spectroscopy was acquired on a Horiba LabRAM HR Evolution using an excitation wavelength of 473 nm in 0.5 M H_2SO_4 solution. The spectral resolution was ~1 cm^{-1}, and the spectral shifts were calibrated routinely via a silicon wafer (520.7 cm^{-1}). The *in situ* Raman experiments were performed in a homemade cell, consisting of a working electrode, a graphite rod counter electrode and an Ag/AgCl (saturated KCl) reference electrode. The XAS spectra were tested at the home-made laboratory-based X-ray absorption spectrometer of the SuperXAFS M9000, the BL14W1 and BL20U beamlines of the Shanghai Synchrotron Radiation Facility (SSRF), and the TPS 44 A beamline of the National Synchrotron Radiation Research Centre (NSRRC). The storage ring of the SSRF was operated at 3.5 GeV with a maximum current of 260 mA, and the TPS was operated at 3.0 GeV with a ring current of 500 mA. The measured spectra were processed and analysed using ATHENA and ARTEMIS (Demeter software package).[3] The Co $L_{2,3}$-edge and Ru L_3-edge data were collected at the TLS 11 A and TLS 16 A beamlines of the NSRRC. *In situ* SR-based XRD data were acquired at the 01C2 beamline in the NSRRC. The XRD experiments were performed at an incident beam energy of 18 keV (λ = 0.68881 Å) using a mar345 image plate area detector. The diffraction intensity and peak shape were calibrated with a CeO_2 reference sample. *In situ* XAS an XRD measurements were conducted in a self-assembled Teflon cell sealed with a Kapton tape window (1 cm × 1 cm). The incident X-ray beam was transmitted through the Kapton window and the electrolyte to collect data signals. All *in situ* experiments were conducted in a standard three-electrode system using a CHI 660 electrochemical workstation.

Electrochemical measurements

All the electrochemical measurements were conducted using a Metrohm Autolab electrochemical workstation with a PGSTAT 302N system. The electrochemical analysis was carried out at room temperature in 0.5 M H_2SO_4 saturated with H_2 for 30 min before each test. The ink of the as-prepared powder catalyst was produced as follows: 5 mg of CCRO powder and 5 mg of carbon black or 5 mg of 20% Pt/C were dispersed in a mixed solution containing 700 μL of deionized water, 250 μL of isopropanol, and 40 μL of Nafion via sonication, resulting in a homogeneous mixture. In this work, isopropanol served as a dispersant agent. Nafion solution served as a dispersant and binding agent and affected proton transfer. A volume of 40 μL of the ink was dropped onto carbon paper (surface area: 1 cm^{-2}, catalyst loading: 0.2 mg cm^{-2}) for use as a working electrode. A graphite rod and Ag/AgCl (saturated KCl solution) were used as the counter and reference electrodes, respectively. A traditional five-port electrolytic cell was used in the three-electrode test. All applied potentials were converted to RHE according to E (RHE) = E (Ag/AgCl) + 0.0591×pH + 0.197 V, and 95% iR-corrected on the basis of the resistance of the electrolyte. LSVs were recorded at a scan rate of 5 mV s^{-1}. The pristine CCRO catalyst was activated using the timed potentiostatic method at a potential of −0.04 V (vs. RHE). In addition, the ECSA of catalysts was estimated using a CV method, which was carried out at different scan rates of 20, 40, 60, 80, and 100 mV s^{-1} within a potential range from −0.15 V to −0.05 V (vs. Ag/AgCl).

The electrochemical C_{dl} was calculated using the following equation:

$$C_{dl} = \frac{j_a - j_c}{2v} = \frac{j_a + |j_c|}{2v} = \frac{\Delta j}{2v}$$

where j_a and j_c are the anodic and cathodic voltammetric current densities, respectively, recorded at the middle of the selected potential range, and v is the scan rate.

The corresponding ECSA were calculated using the following equation:

$$ECSA = \frac{C_{dl}}{C_s}$$

where Cs is a reported constant of 0.04 mF cm^{-2}.

The corresponding TOF values were calculated using the following equation:

$$TOF = \frac{I}{x \times n \times F}$$

where I is the current, x refers to the number of electrons transfer (which is 2 in HER), n refers to the number of Ru/Pt (moles) in catalysts, and F is the Faraday constant (96485 C mol^{-1}). Here, it is assumed that all Ru/Pt atoms in the catalysts participate in the HER process.

The corresponding MA were calculated using the following equation:

$$MA = \frac{j}{m(Ru)}$$

where j represents the current density, m(Ru) represents the mass of Ru, which was determined based on the results obtained from ICP-MS analysis. Based on the stoichiometry of CCRO (Ca_2CoRuO_6), the theoretical Ru mass content is 30.0% of the total catalyst mass. The total CCRO loading was 0.2

mg cm^{-2}. Therefore, the theoretical Ru loading for both pristine and activated CCRO electrodes was 0.06 mg_{Ru} cm^{-2}. According to the ICP-MS results, the value of m(Ru) was 0.059 mg_{Ru} cm^{-2} for the pristine CCRO. This value decreased to 0.046 mg_{Ru} cm^{-2} for the activated CCRO, due to partial dropping-off of the sample during the experimental process. Thus, the actual Ru mass contents for the pristine and activated CCRO catalysts were 97.46% (0.059/0.06) and 76.24% (0.046/0.06), respectively, relative to the theoretical value.

The quantitative analysis of Ru (*n/m*) content in both the pristine and activated CCRO catalysts was performed using the ICP-MS method to accurately determine the Ru (*n/m*) amount for TOF and MA calculations. For the ICP-MS analysis, the samples were placed in polytetrafluoroethylene vessels, and 5 mL of aqua regia was added at room temperature. The vessels were subsequently transferred to a microwave digestion system (ETHOS One). The aqua regia was prepared by mixing concentrated hydrochloric acid (HCl) and concentrated nitric acid (HNO_3) in a volumetric ratio of 3:1. Microwave digestion was performed at a constant temperature of 185°C for a duration of 30 minutes.

The EIS was conducted at an overpotential of −10 mV over a frequency range of 0.1 to 10^5 Hz. All the electrochemical tests were carried out under ambient conditions. The stability test for CCRO by chronopotentiometry at 1 A cm^{-2} was conducted in 0.5 M H_2SO_4 aqueous solution for 200 hours.

For the hydrogen spillover experiment, the activated CCRO catalyst was ultrasonically detached from carbon paper and subsequently dried to collect powder (~2 mg). The powder was then mixed with WO_3 powder (40 mg) for testing. For comparison, tests were also conducted using the same mass of the pristine CCRO powder mixed with WO_3 powder, as well as 40 mg of WO_3 powder alone.

For the CV analysis of the HER effect experiment, 5 mg of CCRO, or 4 mg of CCRO + 1 mg of WO_3, or 5 mg of WO_3 powder was separately mixed with 5 mg of carbon black, and then dispersed in a mixed solvent consisting of deionized water (700 μL), isopropanol (250 μL), and Nafion (40 μL). Following ultrasonic treatment, 40 μL of the ink was carefully loaded onto carbon paper to obtain the corresponding working electrode. The HER treatment of CCRO, CCRO+WO_3, and WO_3 electrodes was obtained by conducting over 50 CV cycles within a potential range of −0.6 V to 0.1 V (vs. RHE), and the scanning rate was 5 mV s^{-1}. In addition, before HER treatment corresponds to the CV test of the pristine CCRO (CCRO+WO_3 or WO_3). After HER treatment corresponds to the CCRO (CCRO+WO_3 or WO_3) after 50 CV cycles, which also represents the activated CCRO.

Electrochemical measurements in PEMWEs.

The Nafion 117 membranes were sequentially treated with 3 wt% H_2O_2, deionized water and 0.5 M H_2SO_4 at 80 °C for 1 hour. After cooling to room temperature, the treated Nafion 117 membranes were washed and preserved in deionized water. CCRO and commercial 20% Pt/C were used as the cathode materials. Commercial 20% Ir/C were used as anode materials. The geometric area of the PEMWE was 4 cm^2 (2 cm × 2 cm). Ti felt (0.25 mm) and carbon paper (0.19 mm) were employed as the anode and cathode gas diffusion layers (GDL) in the PEMWE, respectively.

Preparation of anode and cathode catalyst inks: The catalyst was dispersed in a mixture of isopropanol and 5 wt% Nafion solution. After one hour of ultrasonic treatment, a uniform catalyst ink was obtained. Then, the anode and cathode catalyst inks were directly deposited onto both sides of the Nafion 117 membrane using an ultrasonic spraying system. The catalyst loading on both the anode and cathode was maintained at 2.0 mg cm^{-2}.

The cathode and anode of the PEMWE consist of Ti plates (bipolar plates) featuring serpentine flow channels. The membrane is sandwiched between a porous Ti GDL on the anode side and a carbon paper GDL on the cathode side. During testing, hot deionized water was flowed through the PEMWE at a flow velocity of 30 mL min^{-1}. The temperature of the PEMWE was measured as 60 °C. The I–V curves of the PEMWEs were measured within the current density range of 0–1.2 A cm^{-2} at a voltage sweep rate of 20 mV s^{-1}.

Computational details

All calculations were performed using the Vienna ab initio simulation package (VASP) to implement the DFT of the projected augmented wave (PAW) and the spin-polarized plane wave base set.[4,5] Based on the (010) plane of CCRO perovskite structure, a Co-Ru cluster structure model was established on top of the plane. In this model, the CCRO layer consists of four alternating Co/Ru layers and Ca layers. The Co-Ru cluster comprises two Ru atom layers, containing 16 and 9 Ru atoms respectively. In accordance with the proportion of Co atoms obtained from EDX analysis, one Ru atom in the top Ru layer is substituted with a Co atom. The H $1s^1$, O $2s^22p^4$, Co $4s^23d^7$, and Ru $5s^14d^7$ states were treated as valence electrons. The electronic wave functions were expanded in plane waves using an energy cut-off of 520 eV, and the force and energy convergence criteria were set to 0.05 eV $Å^{-1}$ and 10^{-4} eV, respectively. To address the self-interaction error of the exchange correlation functional, we employed the Hubbard U model to describe the strong correlation of the localized Co 3d states and set the value of U_{eff} = (U − J) to 3.50 eV. The k-point sampling adopted only the gamma point, which is sufficient to simulate this large oxide-support model. The free energy (ΔG) was computed via the following equation:

$$\Delta G = \Delta E + \Delta ZPE - T\Delta S$$

where ΔE is the energy difference of a given reaction, ΔZPE is the zero-point energy correction, and ΔS is the vibrational entropy change at a given temperature T (298.15 K is selected here). The free energy of ($H^+ + e^-$) under standard conditions is assumed to be equal to the energy of 1/2 H_2.

To explore the hydrogen spillover mechanism in Co-Ru/CCRO, a distinct metal/oxide interface model is used, with Co-doping Ru metal cluster containing 9 atoms loading on the (001) CCRO surface slab. The two atomic layers at the bottom of the CCRO slab are fixed to mimic bulk structure, and a ~20 Å-thick vacuum layer was added to reduce dispersive error. Transition states were searched using climbing image nudge elastic band method with 5 images.[6]

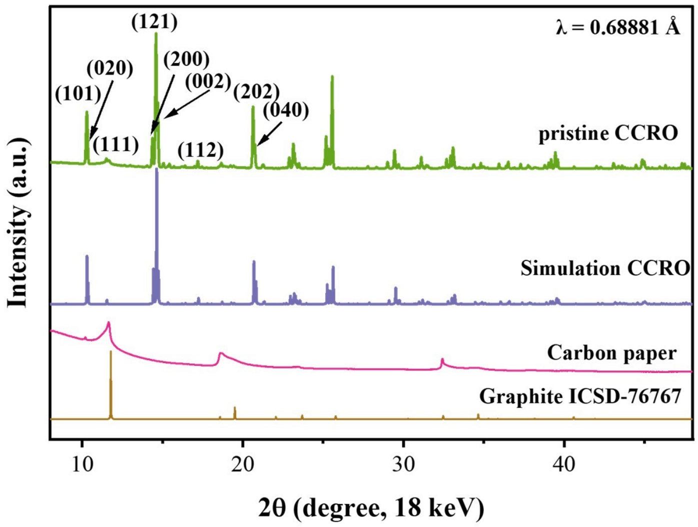

Figure S1. SR-based XRD patterns of the pristine CCRO.

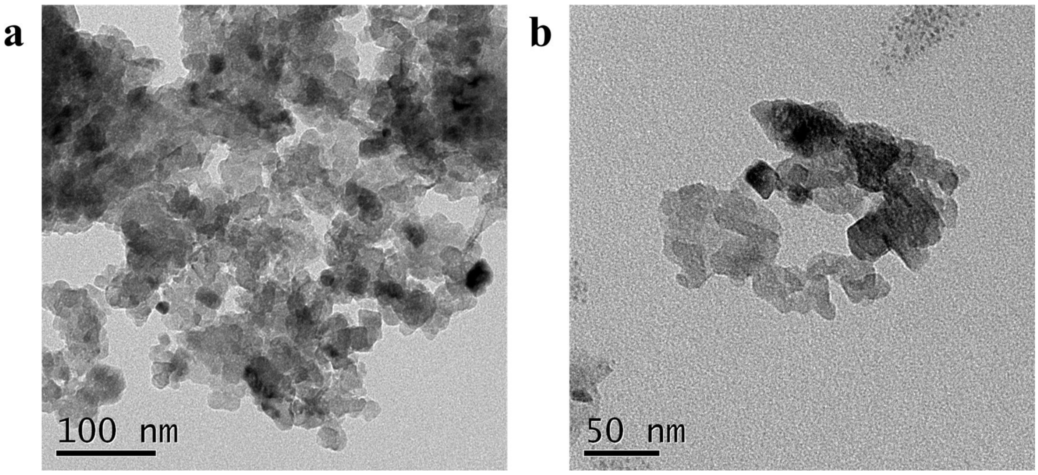

Figure S2. HRTEM images of pristine CCRO.

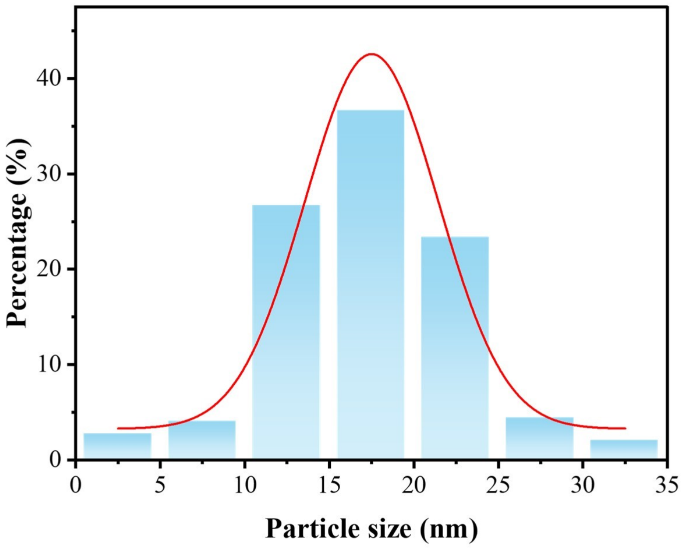

Figure S3. Particle size distribution was determined using the diameters measured on the HRTEM image (Fig. 1c).

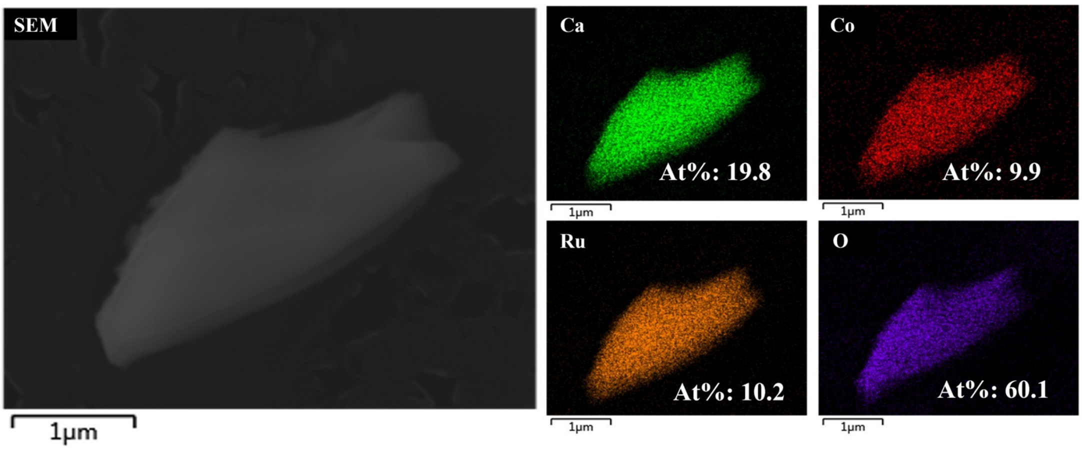

Figure S4. EDX elemental mapping of the pristine CCRO (SEM).

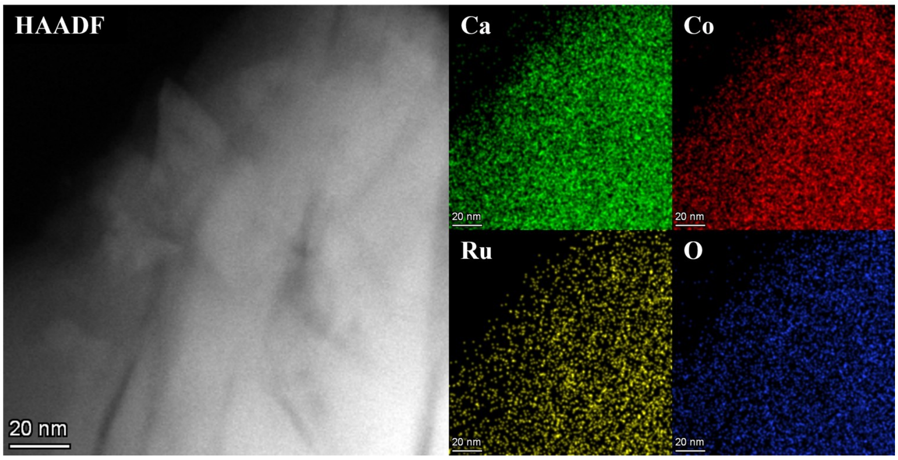

Figure S5. EDX elemental mapping of the pristine CCRO (STEM).

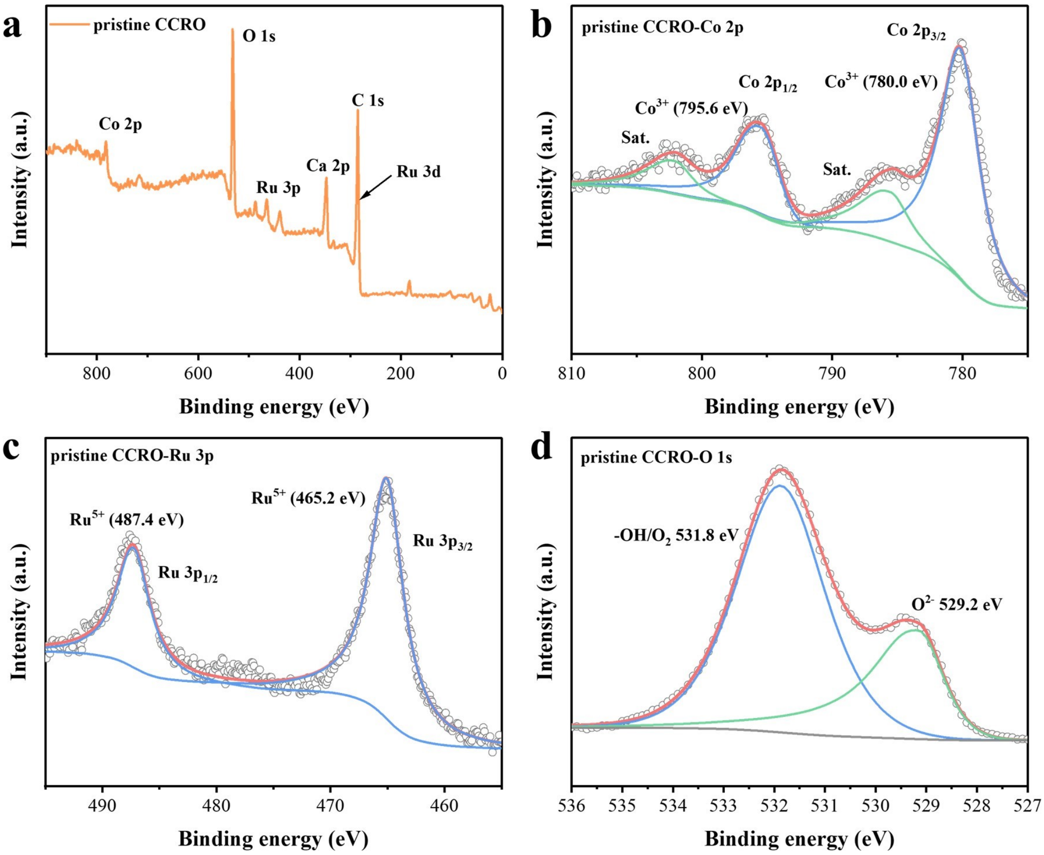

Figure S6. High-resolution XPS spectra of **(a)** survey spectrum, **(b)** Co 2p, **(c)** Ru 3p, and **(d)** O 1s in the pristine CCRO.

For Co 2p and Ru 3p XPS spectra, the peaks at ~780.0 eV ($2p_{3/2}$) and 465.2 eV ($3p_{3/2}$) can be attributed to Co^{3+} and Ru^{5+}, respectively.[7,8] For O 1s XPS spectrum, the peak at ~529.4 eV can be ascribed to the lattice oxygen species (O^{2-}), while that at ~531.4 eV can be attributed to hydroxyl groups or surface-adsorbed oxygen (-OH/O_2).[9]

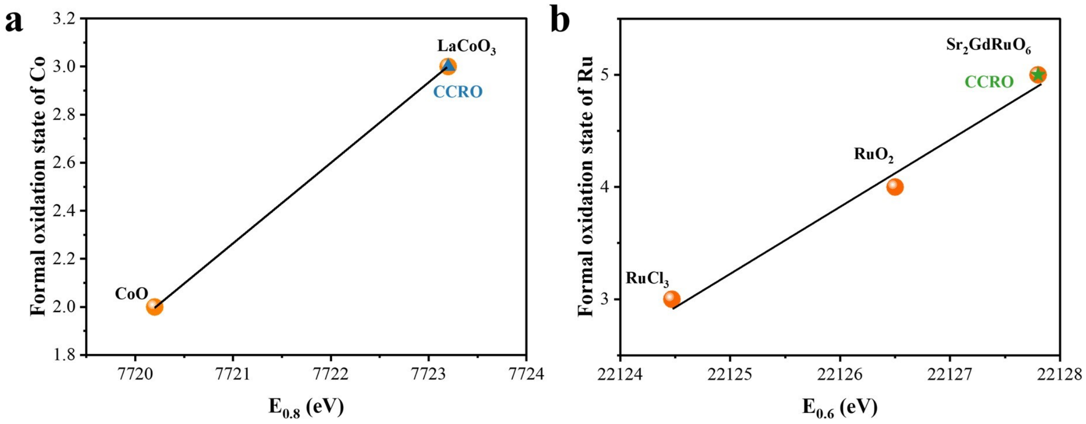

Figure S7. (a) Formal oxidation states of Co as a function of edge energy at 0.8 jump height of the pristine CCRO ($E_{0.8}$), obtained from normalized XANES spectra at the Co *K*-edge. **(b)** Formal oxidation states of Co as a function of edge energy at 0.6 jump height of CCRO ($E_{0.6}$), obtained from normalized XANES spectra at the Ru *K*-edge.

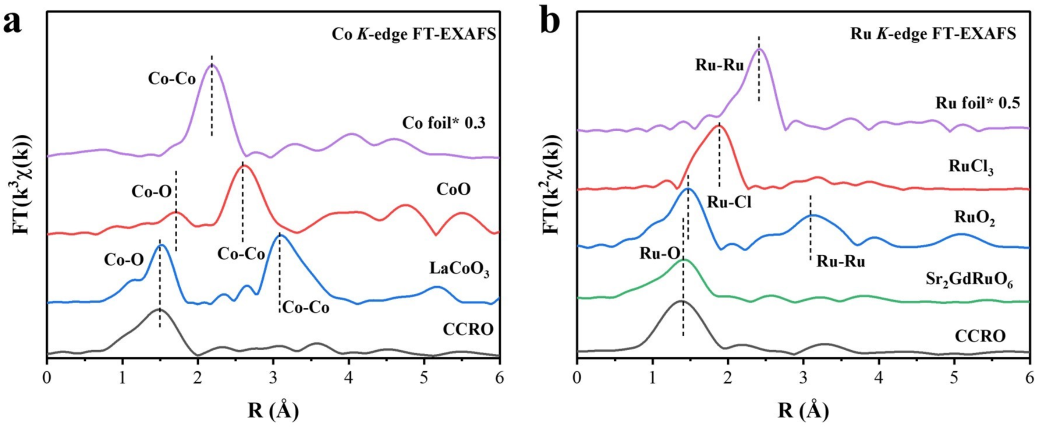

Figure S8. (a) Fourier transforms of k^3-weigted EXAFS spectra at Co K-edge of CCRO, Co foil, CoO and $LaCoO_3$. **(b)** Fourier transforms of k^2-weigted EXAFS spectra at Ru K-edge of CCRO, Ru foil, $RuCl_3$, RuO_2, and Sr_2GdRuO_6.

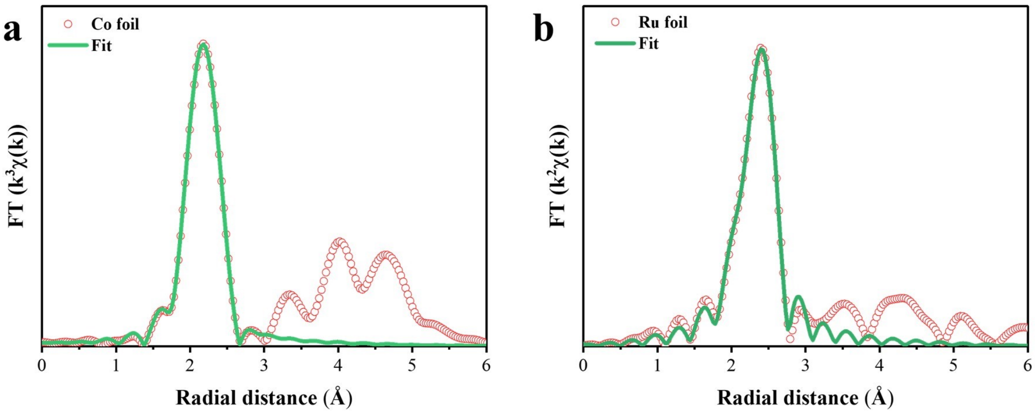

Figure S9. EXAFS fitting results of **(a)** Co foil, and **(b)** Ru foil.

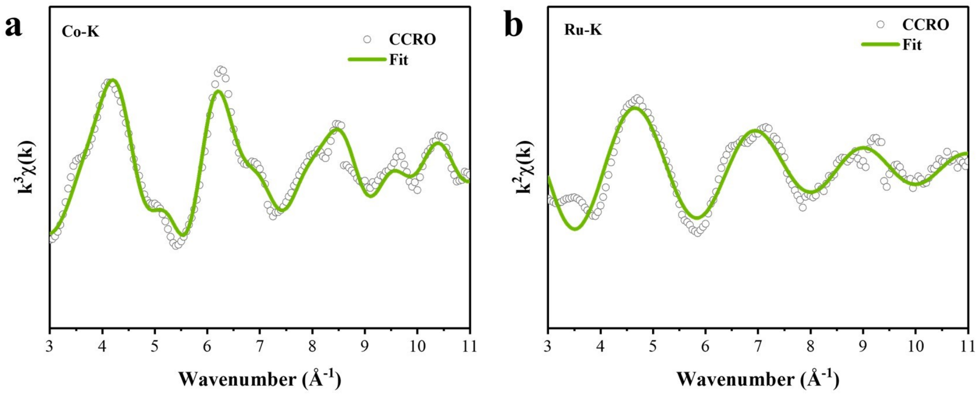

Figure S10. The *k*-space experimental and fitting curves of CCRO at Co and Ru K-edge EXAFS spectra.

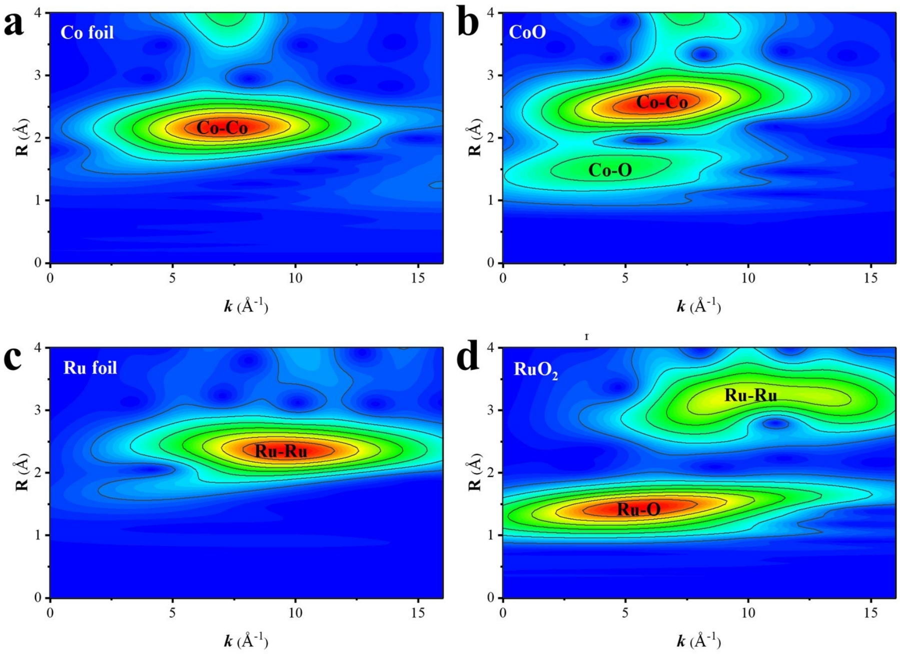

Figure S11. (a) and **(b)** Formal WT plots at Co *K*-edge EXAFS of Co foil and CoO. **(c)** and **(d)** Formal WT plots at Ru *K*-edge EXAFS of Ru foil and RuO_2.

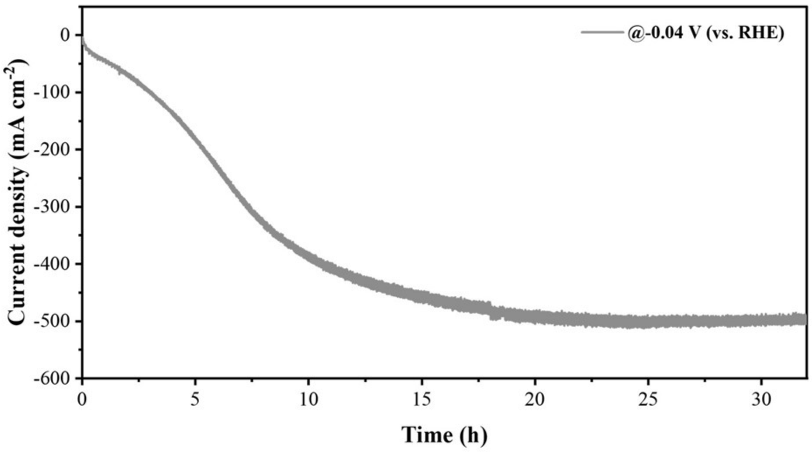

Figure S12. The curve of current density for the pristine CCRO at a potential of −0.04 V (vs. RHE).

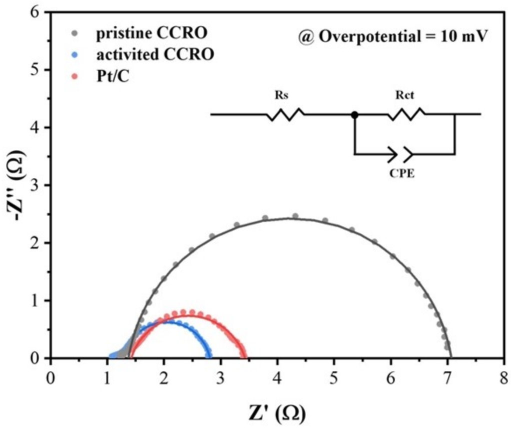

Figure S13. EIS curves of pristine CCRO, activated CCRO, and Pt/C were measured at an overpotential of 10 mV. The charge transfer resistances (R_{ct}) of pristine CCRO, activated CCRO, and Pt/C are 5.7 Ω, 1.5 Ω, and 2.0 Ω, respectively.

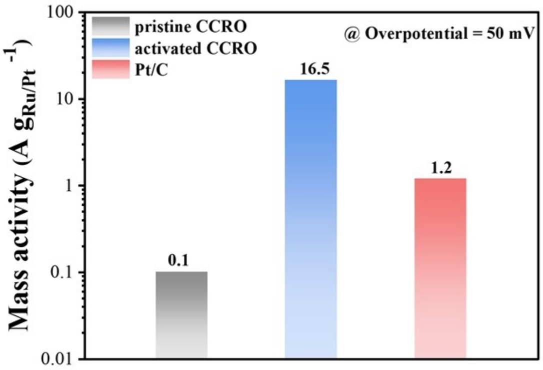

Figure S14. Comparison of mass activities for pristine CCRO, activated CCRO, and 20% Pt/C at an overpotential of 50 mV.

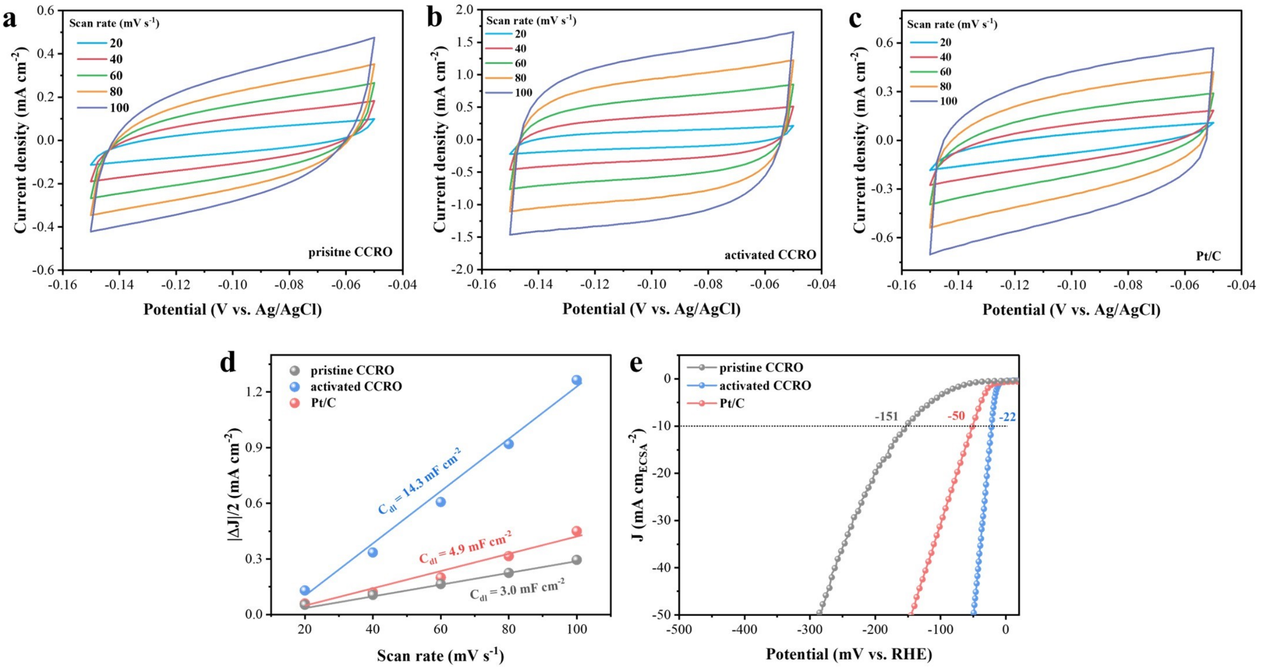

Figure S15. CV curves of **(a)** pristine CCRO, **(b)** activated CCRO, and **(c)** Pt/C recorded at various sweep rates in 0.5 M H_2SO_4. **(d)** ΔJ/2 vs. scan rate plots for pristine CCRO, activated CCRO, and Pt/C. **(e)** LSVs curves normalized by ECSA for pristine CCRO, activated CCRO, and Pt/C.

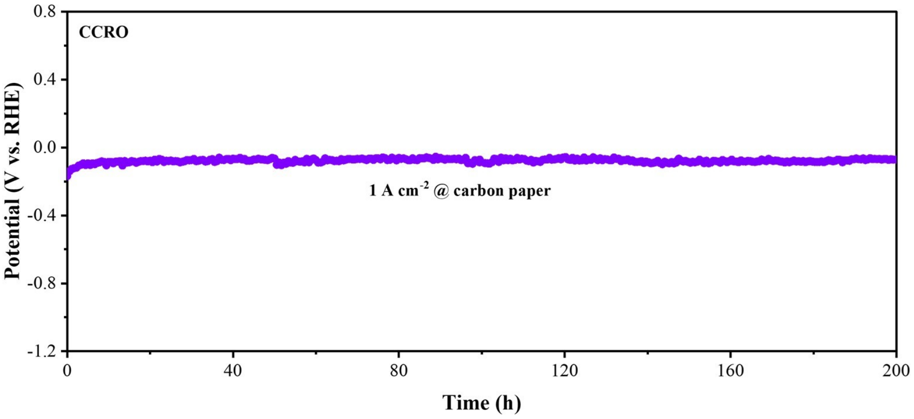

Figure S16. Measurement of the long-term electrochemical stability of CCRO-activated at a current density of 1 A cm^{-2}.

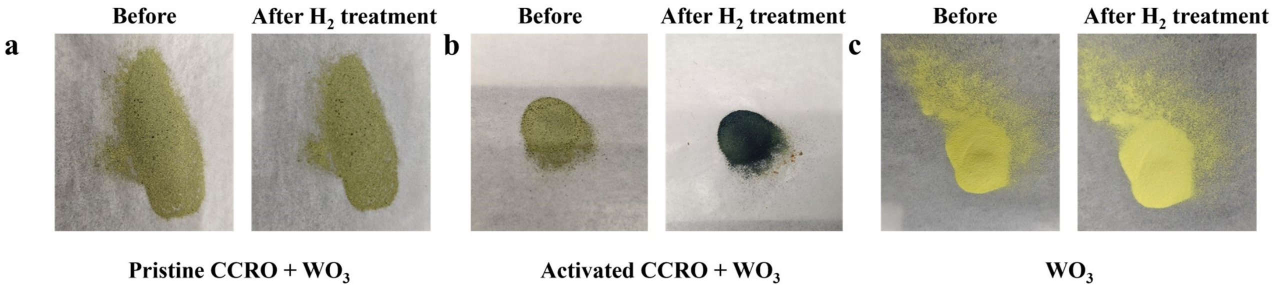

Figure S17. Color change photographs of the mixtures. **(a)** The pristine CCRO+WO_3 before and after H_2 treatment at room temperature. **(b)** The activated CCRO+WO_3 before and after H_2 treatment at room temperature. **(c)** The WO_3 film and WO_3 before and after H_2 treatment at room temperature.

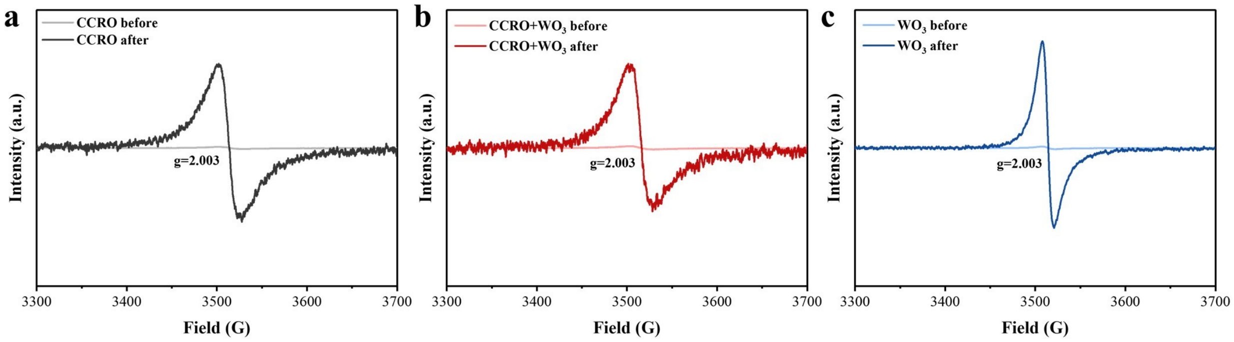

Figure S18. EPR spectra of **(a)** CCRO before and CCRO after, **(b)** CCRO+WO$_3$ before and CCRO+WO$_3$ after, and **(c)** WO$_3$ before and WO$_3$ after.

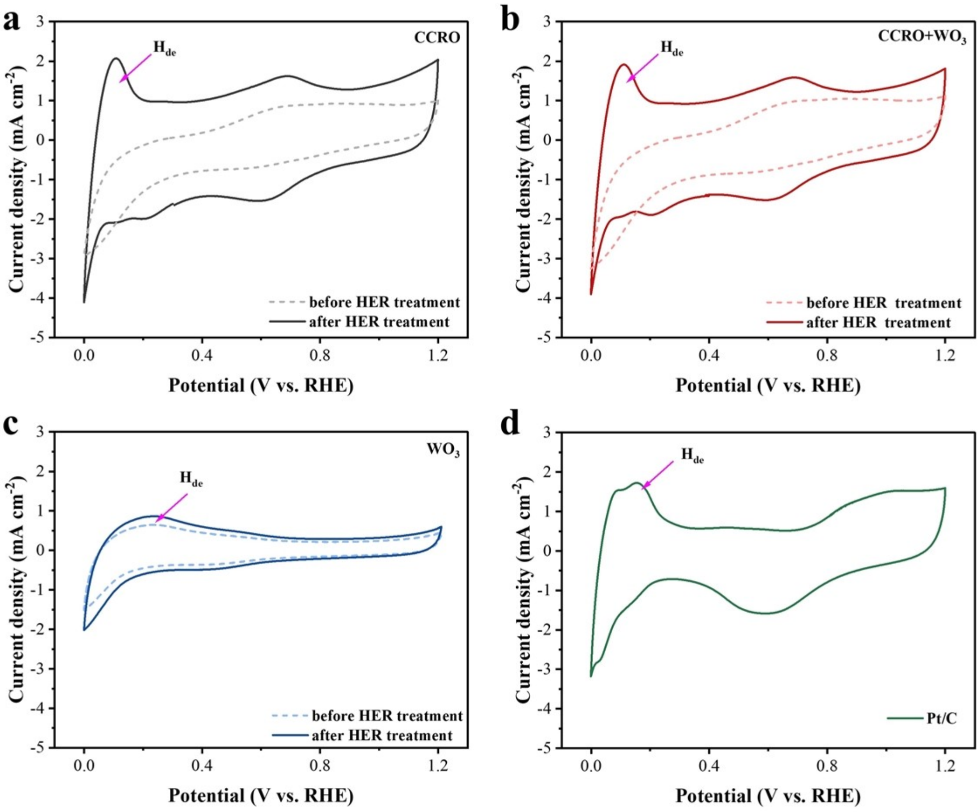

Figure S19. CVs of **(a)** CCRO before (dashed line) and after (solid line) HER treatment, **(b)** CCRO+WO_3 before and after HER treatment, **(c)** WO_3 before and after HER treatment, and (**d**) Pt/C. The scanning rate was 50 mV s^{-1}.

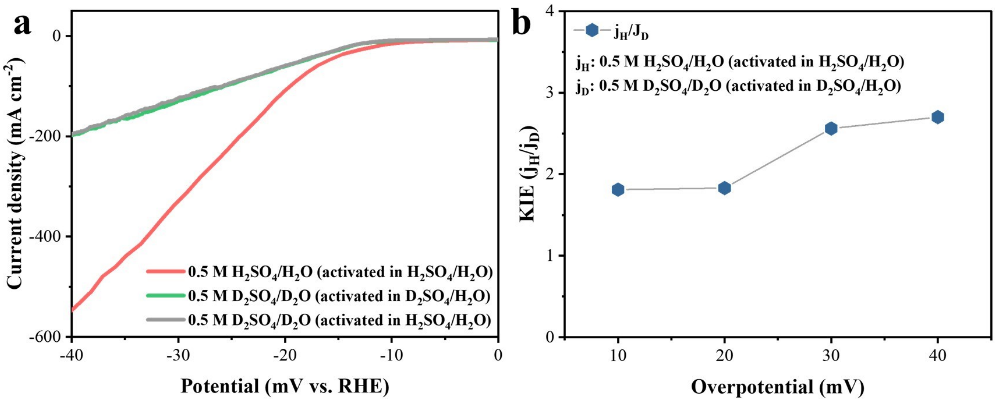

Figure S20. (a) Polarization curves of CCRO catalyst in aqueous 0.5 M H_2SO_4 (activated in H_2SO_4/H_2O), 0.5 M D_2SO_4 (activated in D_2SO_4/D_2O), and 0.5 M D_2SO_4 (activated in H_2SO_4/H_2O) solutions. **(b)** the kinetic isotope effect value of overpotential.

The j_H and j_D represent the current densities of CCRO in H_2SO_4/H_2O and D_2SO_4/D_2O solutions, respectively. The procedure is analogous to the method used for activating and testing CCRO in 0.5 M H_2SO_4. The pristine CCRO was activated in 0.5 M D_2SO_4 and then tested.

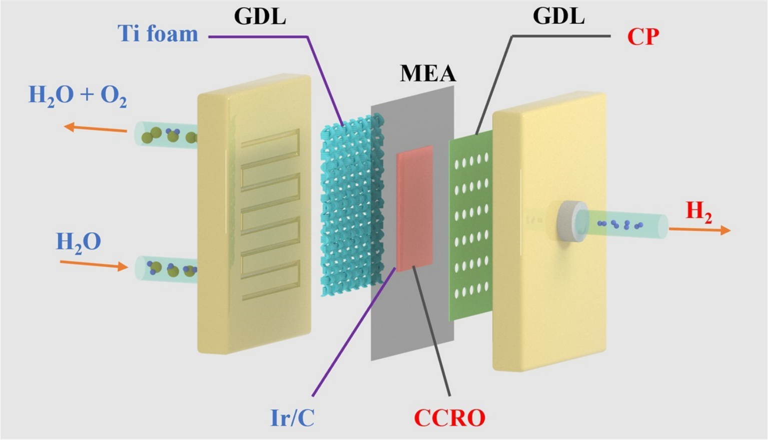

Figure S21. Schematic diagram of the PEMWE.

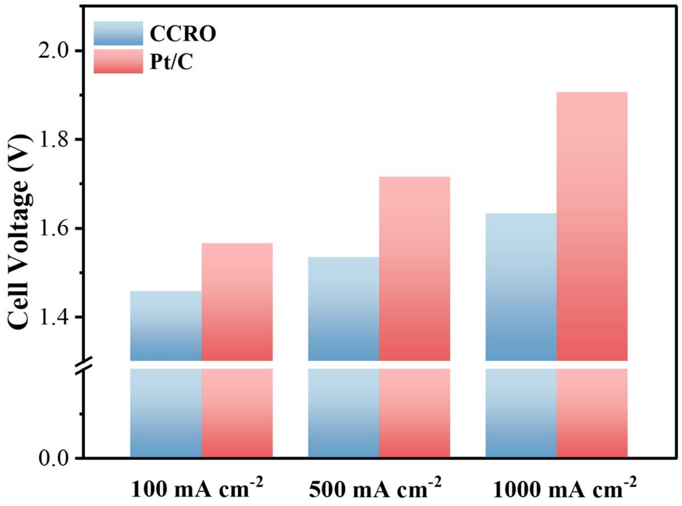

Figure S22. Comparison between the cell voltages (at 100 mA cm^{-2}, 500 mA cm^{-2}, and 1000 mA cm^{-2}) of the CCRO and 20% Pt/C.

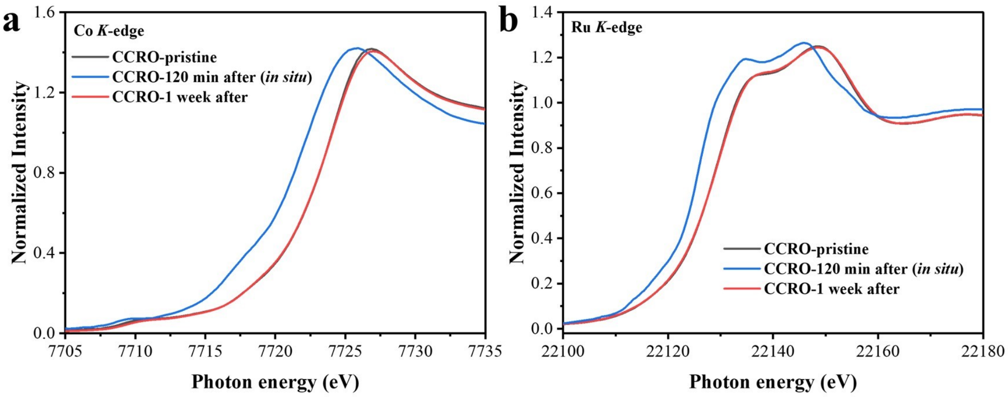

Figure S23. Co-*K* and Ru XANES spectra of CCRO-pristine, CCRO-120 min after (*in situ*), and CCRO-1 week after.

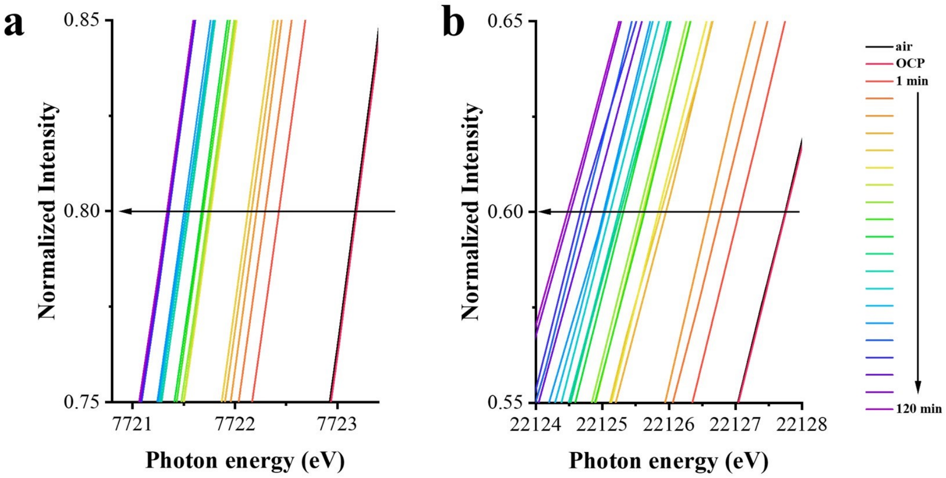

Figure S24. Enlarged segments of time-dependent **(a)** Co *K*-edge, and **(b)** Ru *K*-edge XANES spectra of CCRO. The time interval between each data point is six minutes.

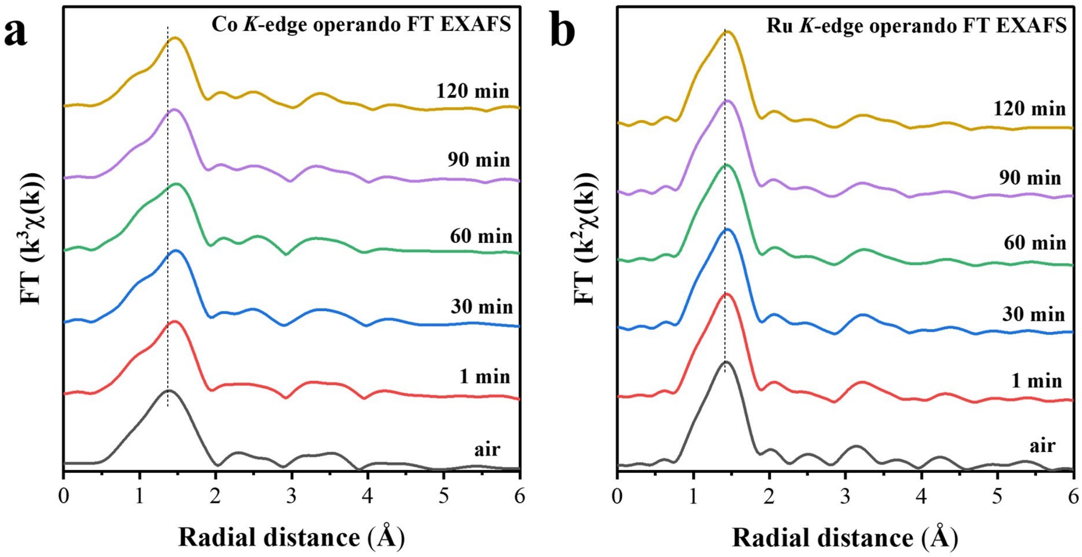

Figure S25. The time-dependent FT-EXAFS at **(a)** Co *K*-edge, and **(b)** Ru *K*-edge of CCRO.

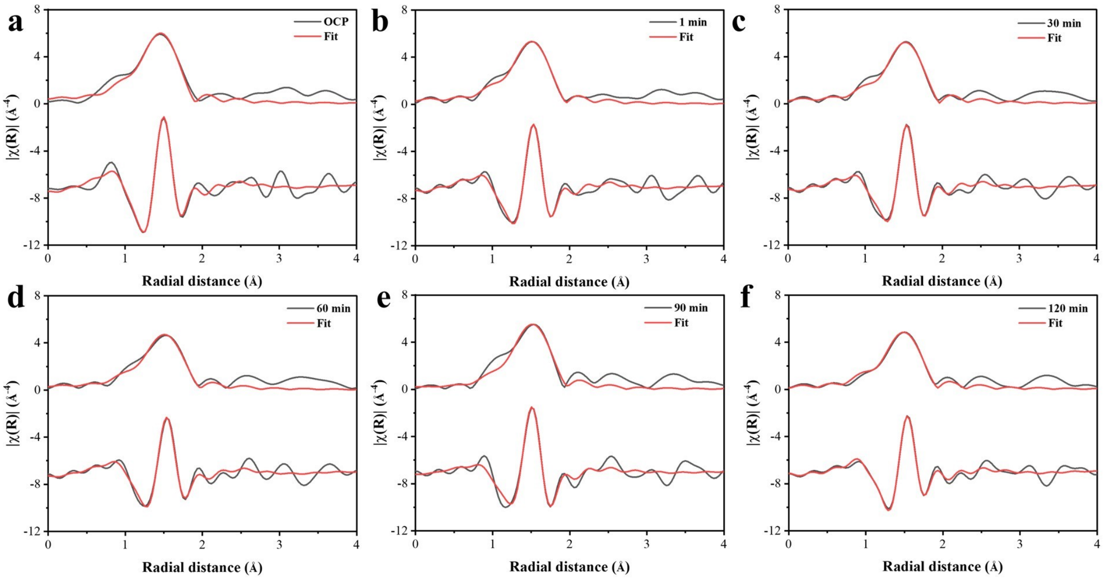

Figure S26. (a-f) Fits for the time-dependent Co *K*-edge spectra of the CCRO measured in 0.5 M H_2SO_4 electrolyte.

In the Figures, the black curves represent the experimental data, whereas the red curves indicate the fitted data. The upper portion of the figures corresponds to the *R*-space data, while the lower portion illustrates the real part of the *R*-space data.

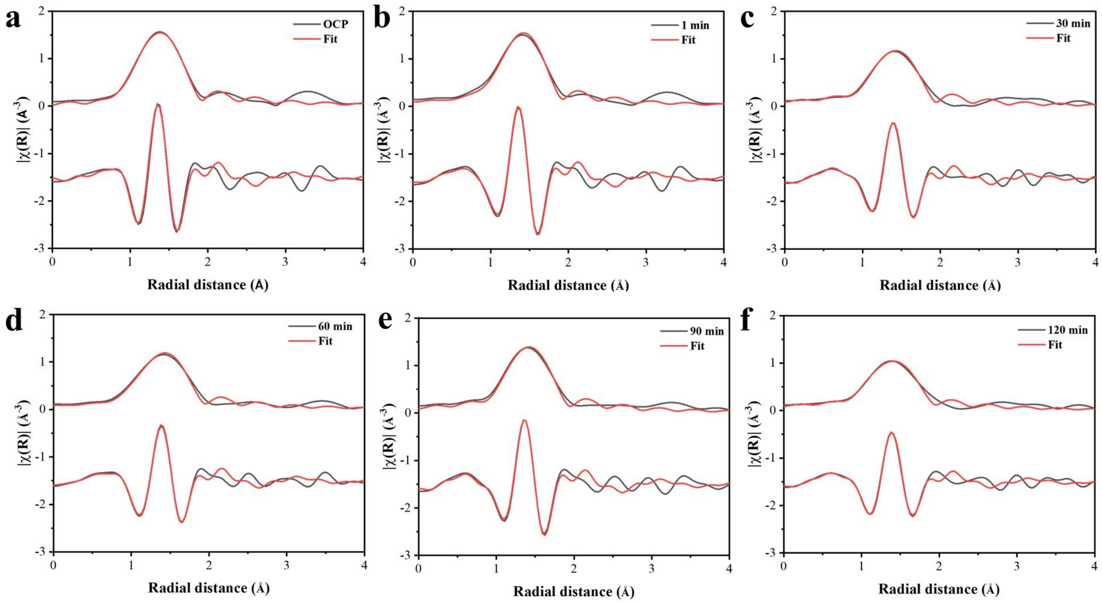

Figure S27. (a-f) Fits for the time-dependent Ru *K*-edge spectra of the CCRO measured in 0.5 M H_2SO_4 electrolyte.

In the Figures, the black curves represent the experimental data, whereas the red curves indicate the fitted data. The upper portion of the figures corresponds to the *R*-space data, while the lower portion illustrates the real part of the *R*-space data.

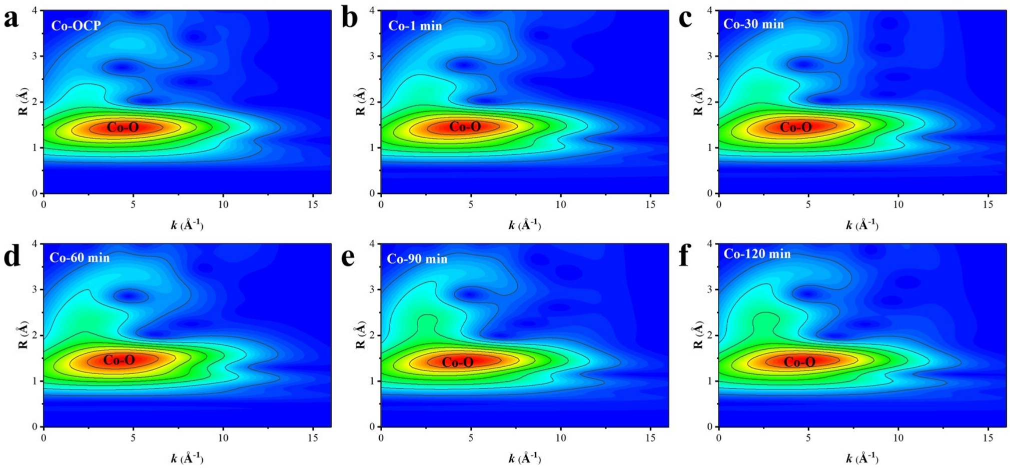

Figure S28. (a-f) Time-dependent WT plots of Co *K*-edge in CCRO.

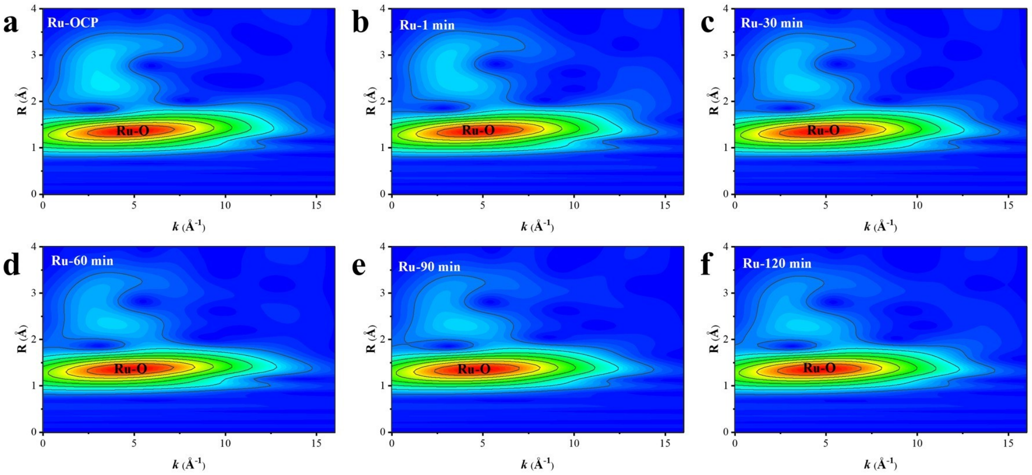

Figure S29. (a-f) Time-dependent WT plots of Ru *K*-edge in CCRO.

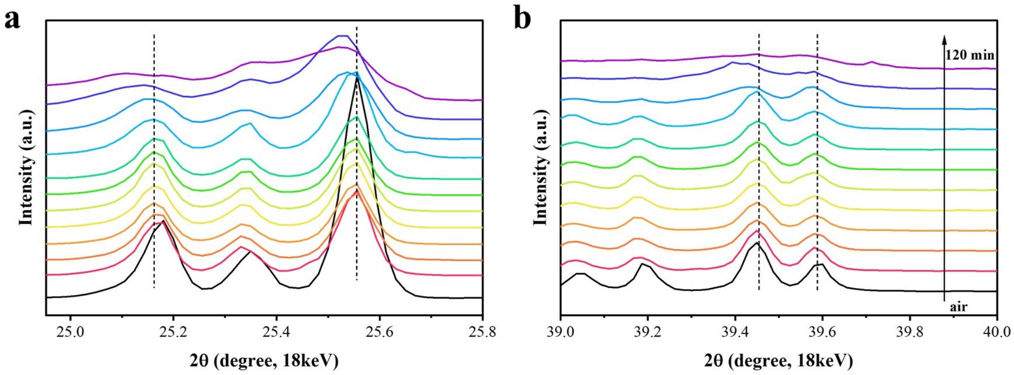

Figure S30. (a and **b)** Enlarged segments of time-dependent XRD diffraction peaks of CCRO.

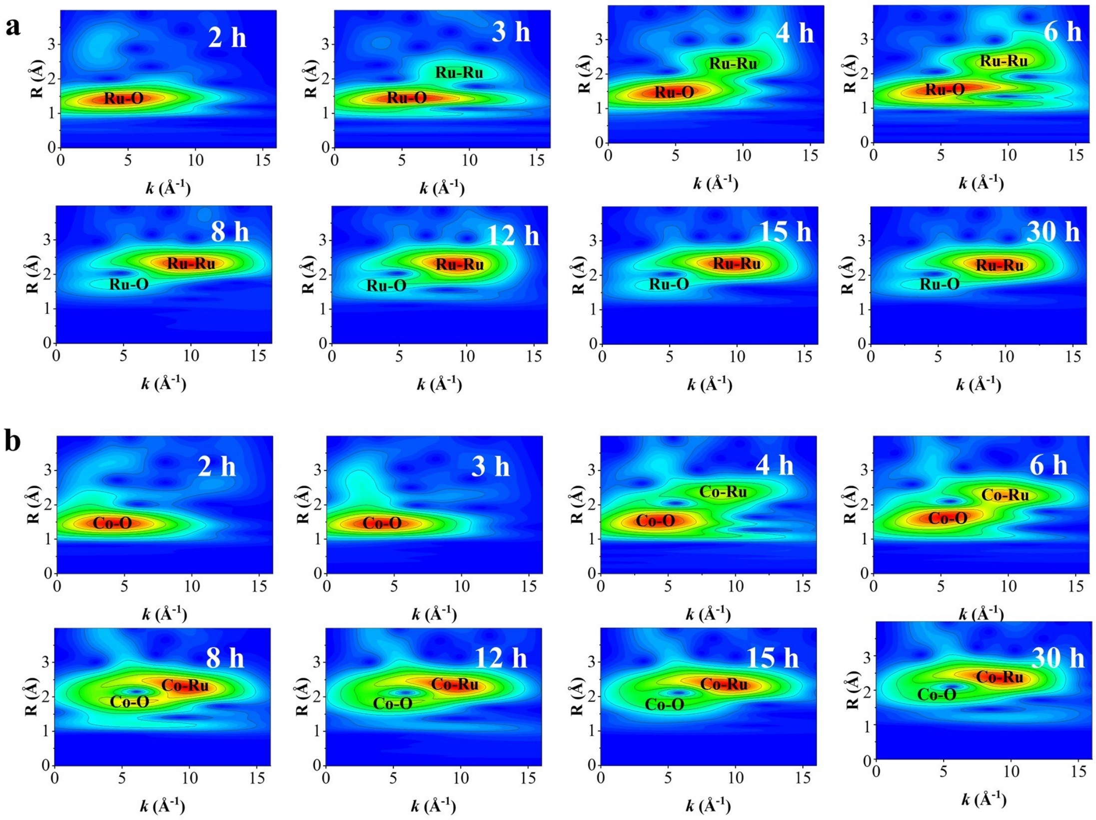

Figure S31. Time dependent WT plots of the **(a)** Ru and **(b)** Co *K*-edge in CCRO from 2 hours to 30 hours.

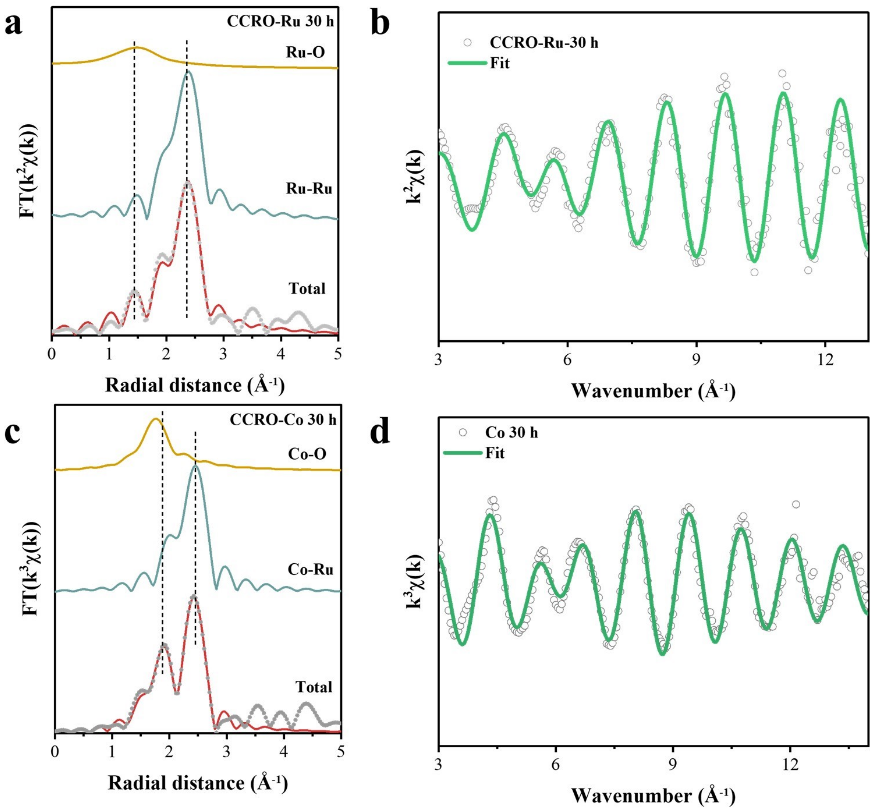

Figure S32. The Ru *K*-edge FT EXAFS spectra of CCRO-Ru 30h in **(a)** *R*- and **(b)** *k*-space. The Co *K*-edge FT EXAFS spectra of CCRO-Co 30h in **(c)** *R*- and **(d)** *k*-space. Measured and calculated spectra are well matched for all samples. The best-fit parameters are shown in Supplementary Table. S9.

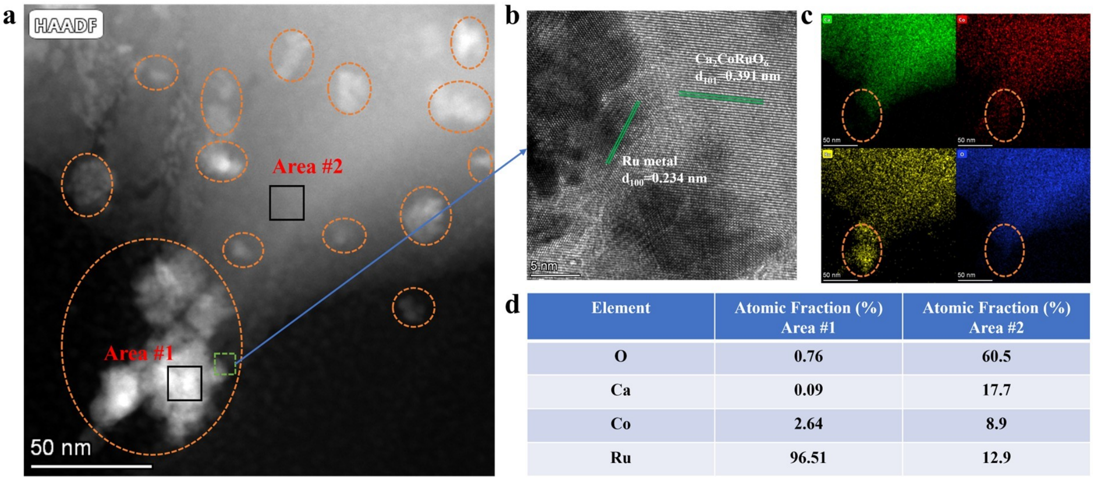

Element	Atomic Fraction (%) Area #1	Atomic Fraction (%) Area #2
O	0.76	60.5
Ca	0.09	17.7
Co	2.64	8.9
Ru	96.51	12.9

Figure S33. (**a**) The HRTEM image of CCRO obtained after 8 hours at a potential of −0.04V (vs. RHE). (**b**) The partially enlarged image shows both the black region and the particle junction (green dot box). (c) The EDX images obtained from Fig. S27a. (d) EDX quantitative analysis was performed separately on Area #1 and Area #2 (black box).

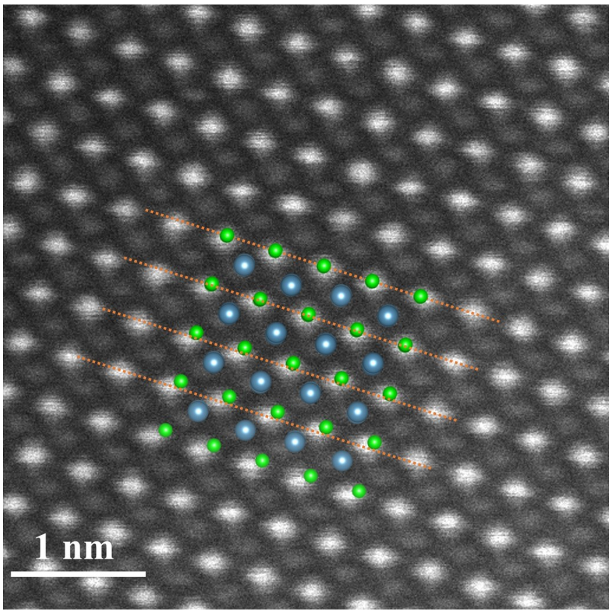

Figure S34. Atomic-resolution HAADF-STEM image of CCRO obtained after 8 hours at a potential of −0.04 V (vs. RHE). The green and azure dots represent the Co/Ru and Ca atoms, respectively. After 8-hour reaction, the CCRO perovskite substrate undergoes lattice expansion. Consequently, the atomic positions deviate from the original crystal structure model, with the interatomic spacing (lattice fringe spacing) gradually becoming larger than that of the original crystal model.

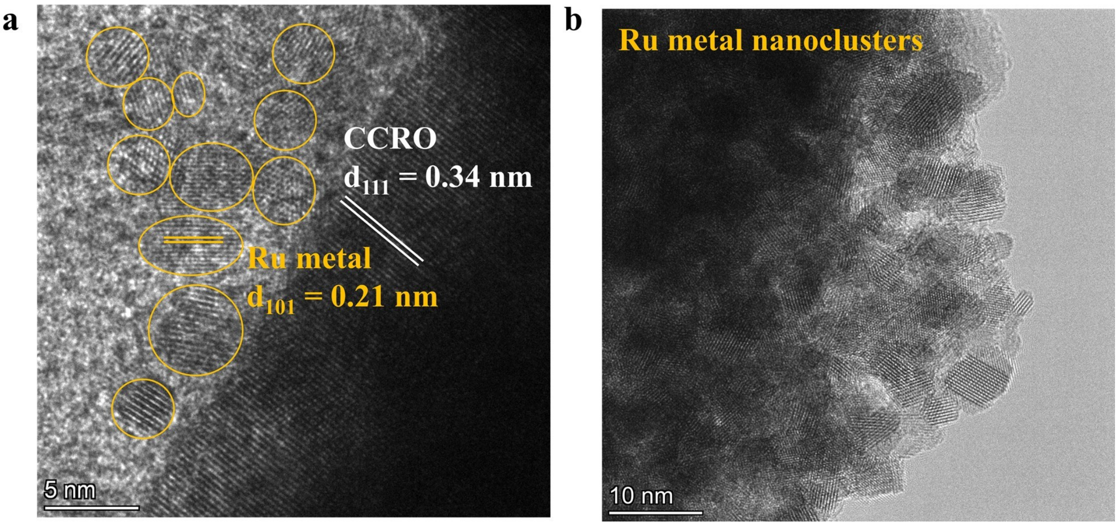

Figure S35. (a) and **(b)** HRTEM images of CCRO catalyst after more than 1,500 hours of reaction in the PEMWE.

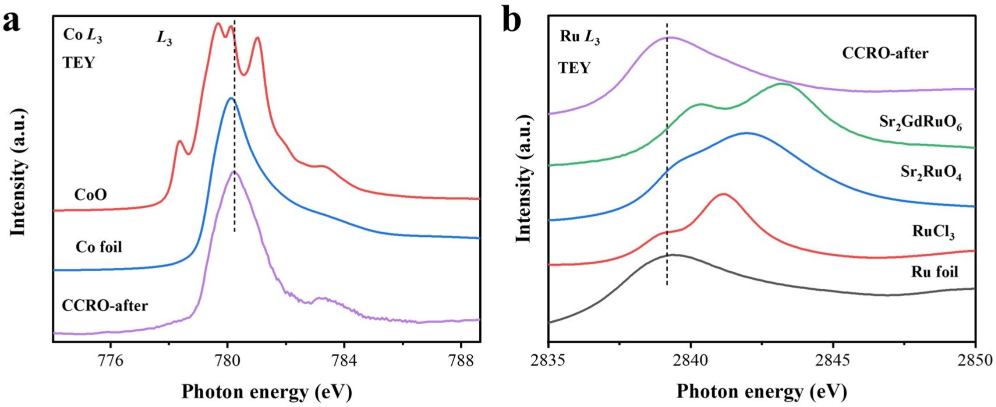

Figure S36. *Ex situ* **(a)** Co and **(b)** Ru L_3-edge of CCRO after the HER for 30 hours.

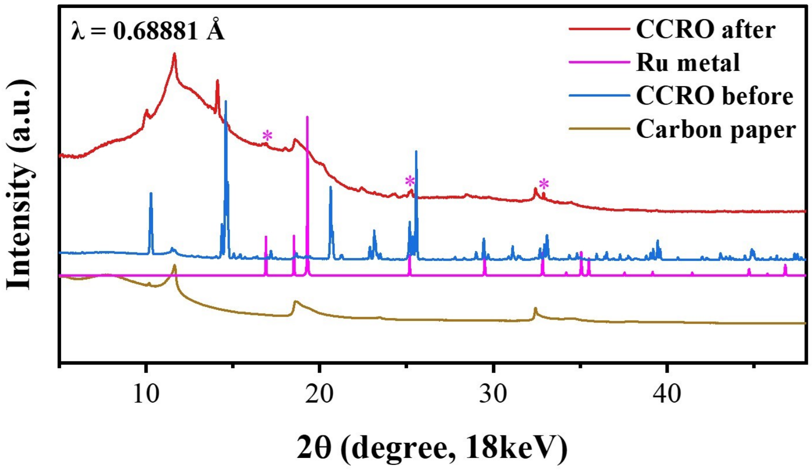

Figure S37. SR-based XRD patterns of CCRO before and after the *in situ* XRD testing.

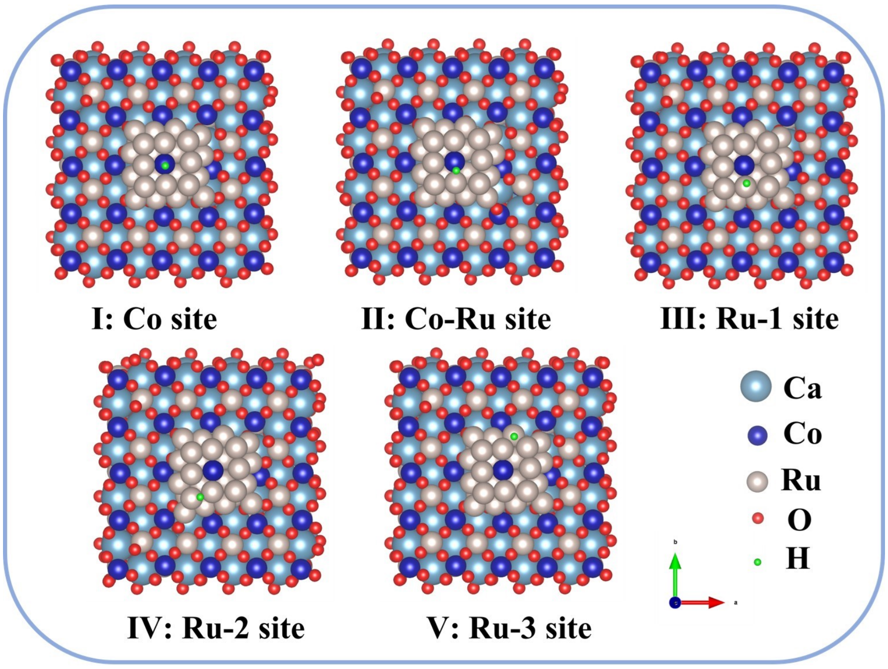

Figure S38. Hydrogen adsorption at different sites of Co-Ru/CCRO structures. The azure, blue, grey, yellow, red, and green balls represent Ca, Co, Ru, Pt, O, and H, respectively.

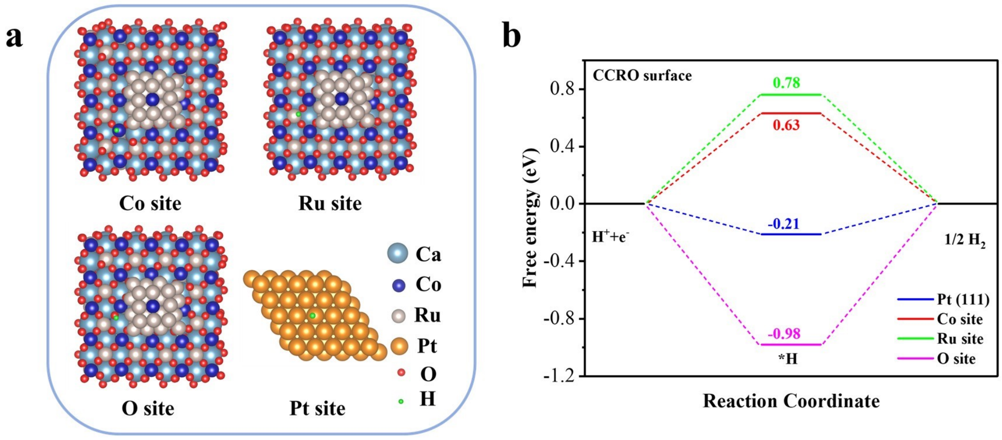

Figure S39. (**a**) Hydrogen adsorption at different sites of Co-Ru/CCRO and Pt (111) structures. The azure, blue, grey, yellow, red, and green balls represent Ca, Co, Ru, Pt, O, and H, respectively. (**b**) The Gibbs free energy diagram for hydrogen adsorption at different sites on CCRO and Pt (111).

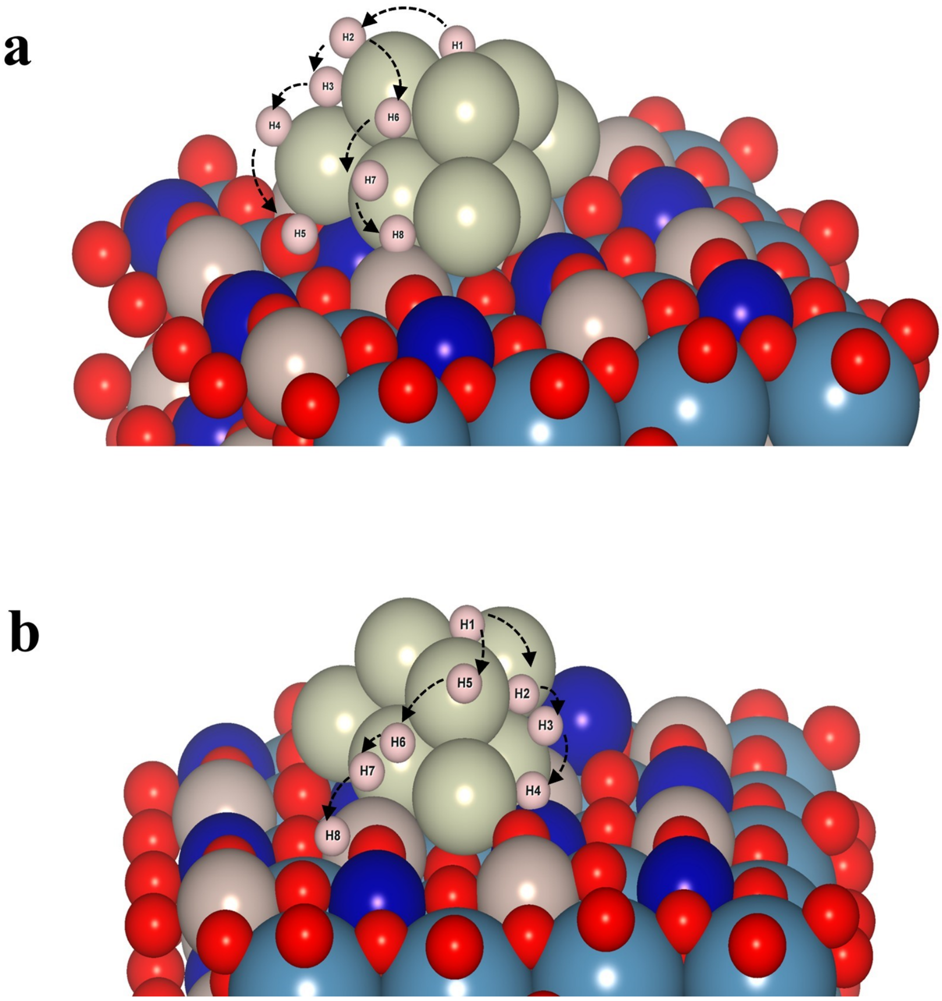

Figure S40. The schematic of hydrogen adsorption sites and the corresponding free energy diagram of hydrogen spillover for **(a)** Ru/CCRO and **(b)** Co-Ru/CCRO. The azure, blue, grey, red, and white balls represent Ca, Co, Ru, O, and H, respectively.

Table S1. The refined **(a)** lattice parameters of pristine CCRO, **(b)** atomic parameters of pristine CCRO, and **(c)** crystal planes of pristine CCRO and their corresponding interplanar spacings.

(a) lattice parameters.

Phase type	**Space group**	**a (Å)**	**b (Å)**	**c (Å)**	***V* [Å^3]**
Orthorhombic	*Pnma*	5.4843	7.6246	5.3666	224.41

(b) atomic parameters.

Atom	**site**	***x/a***	***y/b***	***z/c***	***U* [Å^2]**
O2	1	0.20819	0.04389	0.29071	0.0188
Ca	.m.	0.44909	0.25	0.01387	0.0132
O1	.m.	0.51740	0.25	0.58276	0.0250
Ru	-1	0	0	0	0.0007
Co	-1	0	0	0	0.0139

(c) crystal planes of pristine CCRO and their corresponding interplanar spacings.

Crystal plane	Distance (Å)
101	3.84
020	3.81
111	3.43
200	2.74
121	2.70
002	2.68
112	2.30
202	1.92
040	1.91

Table S2. The atomic percentage of each element in the EDX spectrum (from Fig. 1g) of pristine CCRO.

Atom	Family	Atomic Fraction (%)	Atomic Error (%)
Ca	K	20.13	2.13
Co	K	10.07	1.07
Ru	K	10.12	1.34
O	K	59.68	4.33

Table S3. The atomic percentage of each element in the EDX spectrum (from Fig. S4) of pristine CCRO.

Atom	Family	Atomic Fraction (%)	Atomic Error (%)
Ca	K	19.87	3.17
Co	K	9.89	2.15
Ru	K	10.16	4.24
O	K	60.08	5.93

Table S4. EXAFS fitting parameters of the Co/Ru *K*-edge for **(a)** foil and **(b)** pristine CCRO.

(a) Co foil and Ru foil

Sample	Scattering path	*N*	*R* (Å)	$\sigma^2(10^{-3}Å^2)$	S_0^2	*R* factor
Co foil	Co-Co	12*	2.495±0.06	6.5	0.77	0.003
Ru foil	Ru-Ru	6*	2.622±0.03	3.1	0.65	0.007
	Ru-Ru	6*	2.733±0.02	3.3		

(b) pristine CCRO

Sample	Scattering path	*N*	*R* (Å)	$\sigma^2(10^{-3}Å^2)$	*R* factor
CCRO	Co-O	5.8±0.6	1.971±0.03	5.3	0.004
	Ru-O	5.9±0.4	1.953±0.02	3.7	0.016

N: coordination numbers; *R*: bond distance; σ^2: Debye-Waller factor to account for both thermal and structural disorders; Δ*R* factor: goodness of fit. The Fourier-transform window was in the k range 3–11.0 $Å^{-1}$. S_0^2 was fixed to 0.77 and 0.65 of Co and Ru, according to the experimental EXAFS fit of Co/Ru foil by fixing CN as the known crystallographic value.

Table S5. Comparison of HER performance with previous reported high activity Ru-based HER catalysts.

No.	**Catalysts**	$\lvert\eta_{10}\rvert$ **(mV)**	$\lvert\eta_{100}\rvert$ **(mV)**	**Tafel slope (mV dec^{-1})**	**Loading (mg$_{Ru}$ cm^{-2})**	**MA at −50 mV (A mg$_{Ru}$$^{-1}$)**	**Reference**
1	Activated CCRO	7	20	10	0.046	16.52	This work
2	CoRu/NC-700	6	60	21	–	–	[10]
3	RuCoP	11	77	31	0.053	0.79	[11]
4	Ru@MWCNT	13	–	27	0.081	1.56	[12]
5	Ru/NCDs	15	85	25	–	–	[13]
6	RuCu NSs/C-250	19	–	26	0.254	0.14	[14]
7	SL-Ni-Ru-VS$_2$	20	41	34	0.013	18.01	[15]
8	Ru@C$_2$N	22	–	30	0.082	0.37	[16]
10	Ru$_1$Ni$_1$-NCNFs	23	87	29	0.169	0.28	[17]
11	Ru/g-C$_3$N$_4$-2	27	95	22	–	–	[18]
12	0.04-Ru@CN-6	30	65	42	0.024	1.00	[19]
13	RuS$_x$/S-GO	31	50	40	0.443	0.11	[20]
14	Mn(SAs)-Ru/RuO$_2$	39	101	14	0.041	0.95	[21]
15	RuNiS-C	43	75	39	0.043	0.42	[22]
16	Co$_{0.87}$Ru$_{0.13}$/GC	44	115	68	0.004	2.66	[23]
17	NiCoP@Ru	49	72	49	0.112	0.08	[24]
18	Ru/NG-750	54	85	44	0.005	2.03	[25]
19	Ru-MoO$_2$	55	–	44	0.023	0.26	[26]

Table S6. Comparison of HER performance at the current density of 1000 mA cm^{-2} in 0.5 M H_2SO_4 solution.

No.	**Catalyst**	$\|\eta_{1000}\|$ **(mV)**	**Reference**
1	Activated CCRO	62	This work
2	Pt-Er/h-NC	167	[27]
3	SRO single crystals	182	[28]
4	Cr, B-doped RuO_2 NFs	205	[29]
4	MoS_2/Mo_2C	227	[30]
5	P_3-MNS_3/NF	243	[31]
6	Cu-m/Cu-W/NiCo-LDH	246	[32]
7	MoS_2/graphene	250	[33]
8	NiCoP-r	256	[34]
9	MoSx-Fe@UiO-66-$(OH)_2$	297	[35]
10	$Fe_{0.2}Co_{0.8}Se_2$/g-C_3N_4	317	[36]
11	Nb-doped WS_2	320	[37]
13	VS_2/MoS_2/MF	336	[38]
14	Co–NC–AF	343	[39]
15	2H $Nb_{1.35}S_2$	370	[36]
16	$Co_{(10.4)}$/Se-MoS_2-NF	382	[40]
17	HC-MoS_2/Mo_2C	412	[41]
18	MoS_2/CNF-PHH-U	450	[42]

Table S7. *In situ* EXAFS fitting parameters of Co *K*-edge in CCRO catalyst during the HER.

Sample	**Scattering path**	***N***	***R*** **(Å)**	**σ^2(10^{-3}Å^2)**	***R*** **factor**
OCP	Co-O	5.8±0.7	1.968±0.03	9.0	0.004
1 min	Co-O	5.8±0.9	1.972±0.02	8.3	0.006
30 min	Co-O	5.7±0.7	1.978±0.03	7.6	0.005
60 min	Co-O	5.6±1.2	1.986±0.02	9.1	0.008
90 min	Co-O	5.7±1.0	1.993±0.02	7.0	0.005
120 min	Co-O	5.6±1.3	2.001±0.03	8.6	0.005

Table S8. *In situ* EXAFS fitting parameters of Ru *K*-edge in CCRO catalyst during the HER.

Sample	**Scattering path**	***N***	***R* (Å)**	**σ^2(10^{-3}Å^2)**	***R* factor**
OCP	Ru-O	5.7±0.9	1.952±0.02	3.2	0.009
1 min	Ru-O	5.6±1.2	1.968±0.02	3.2	0.015
30 min	Ru-O	5.8±1.4	1.979±0.03	4.9	0.004
60 min	Ru-O	5.5±1.4	1.986±0.02	3.7	0.011
90 min	Ru-O	5.6±1.5	2.001±0.03	6.4	0.007
120 min	Ru-O	5.5±1.7	2.013±0.02	6.2	0.003

Table S9. EXAFS fitting parameters of the Co/Ru *K*-edge were obtained for CCRO after a 30 hours reaction.

Sample	**Scattering path**	***N***	***R*** (Å)	$\sigma^2(10^{-3}Å^2)$	***R* factor**
Co-30 h	Co-O	3.1±0.5	2.032±0.02	3.4	0.008
	Co-Ru	4.9±1.2	2.640±0.02	4.1	
Ru-30 h	Ru-O	4.2±0.9	2.013±0.04	7.0	0.007
	Ru-Ru	8.7±3.2	2.661±0.02	3.2	

References

1 J. Zhao, S.-C. Haw, X. Wang, Z. Hu, C.-Y. Kuo, S.-A. Chen, H. Ishii, N. Hiraoka, H.-J. Lin, C.-T. Chen, Zhi Li, A. Tanaka, C.-E. Liu, R. Yu, J.-M. Chen, C. Jin, *Phys. Status Solidi. B*, 2021, **258**, 2100117.

2 H. Xia, J. Dai, Y. Xu, Y. Yin, X. Wang, Z. Liu, M. Liu, M. A. McGuire, X. Li, Z. Li, C. Jin, Y. Yang, J. Zhou, Y. Long, *Phys. Rev. Mater.*, 2017, **1**, 024406.

3 B. Ravel, M. Newville, *J. Synchrotron Radiat.*, 2005, **12**, 537.

4 G. Kresse, J. Furthmüller, *Comp. Mater. Sci.*, 1996, **6**, 15.

5 G. Kresse, D. Joubert, *Phys. Rev. B*, 1999, **59**, 1758.

6 G. Henkelman, B. P. Uberuaga, H. Jónsson, *J. Chem. Phys.*, 2000, **113**, 9901.

7 Y. Li, H. Zhang, D. Li, J. Xie, A. Chang, *Ceram Int.*, 2024, **50**, 27496.

8 M. Sathiya, K. Ramesha, G. Rousse, D. Foix, D. Gonbeau, A. S. Prakash, M. L. Doublet, K. Hemalatha, J. M. Tarascon, *Chem Mater*, 2013, **25**, 1121.

9 Z. Xia, Y. Zhang, X. Xiong, J. Cui, Z. Liu, S. Xi, Z. Hu, J.-Q. Wang, L. Zhang, *Appl. Catal. B-Environ. Energy*, 2024, **357**, 124314.

10 J. Chen, J. Huang, Y. Zhao, L. Cao, K. Kajiyoshi, Y. Liu, Z. Li, Y. Feng, *Chem. Eng. J.*, 2022, **450,** 138026.

11 J. Xu, T. Liu, J. Li, B. Li, Y. Liu, B. Zhang, D. Xiong, I. Amorim, W. Li, L. Liu, *Energy Environ. Sci.*, 2018, **11**, 1819.

12 D. H. Kweon, M. S. Okyay, S.-J. Kim, J.-P. Jeon, H.-J. Noh, N. Park, J. Mahmood, J.-B. Baek, *Nat. Commun.*, 2020, **11**, 1278.

13 Z. Liu, H. Zhang, D. Liu, Y. Feng, D. Jia, C. Li, Q. Sun, Y. Zhou, Z. Kang, B. Li, *J. Mater. Chem. A*. 2024, **12**, 8707.

14 Q. Yao, B. Huang, N. Zhang, M. Sun, Q. Shao, X. Huang, *Angew. Chem. Int. Ed.*, 2019, **131**, 14121.

15 R. Wang, Q. Chen, X. Liu, Y. Hu, L. Cao, B. Dong, *Small*, 2024, **20**, 2311217.

16 J. Mahmood, F. Li, S.-M. Jung, M. S. Okyay, I. Ahmad, S.-J. Kim, N. Park, H. Y. Jeong, J.-B. Baek, *Nat. Nanotechnol.*, 2017, **12**, 441.

17 M. Li, H. Wang, W. Zhu, W. Li, C. Wang, X. Lu, *Adv. Sci.*, 2020, **7**, 1901833.

18 D. Li, Y. Liu, Z. Liu, J. Yang, C. Hu, L. Feng, *J. Mater. Chem. A*, 2021, **9**, 15019.

19 N. Wang, X. Bo, M. Zhou, *J. Colloid Interface Sci*., 2021, **604**, 885.

20 P. Li, X. Duan, S. Wang, L. Zheng, Y. Li, H. Duan, Y. Kuang, X. Sun, *Small*, 2019, **15**, 1904043.

21 S. Dong, P. Wang, Z. Li, L. Wei, S. Liu, Y. Yang, F. Zheng, *Adv. Funct. Mater*,. 2024, 2422166.

22 T. L. Jin, X. Liu, H. Wang, X. Wu, Y. Zhang, *Carbon*, 2020, **162**, 172-180.

23 S. Zhang, Y. Rui, X. Zhang, R. Sa, F. Zhou, R. Wang, X. Li, *Chem. Eng. J*., 2021, **417**, 128047.

24 S. Liu, Q. Liu, Y. Lv, B. Chen, Q. Zhou, L. Wang, Q. Zheng, C. Che, C. Chen, *Chem. Commun*., 2017, **53**, 13153.

25 R. Ye, Y. Liu, Z. Peng, T. Wang, A. S. Jalilov, B. I. Yakobson, S.-H. Wei, J. M. Tour, *ACS Appl. Mater. Inter*., 2017, **9**, 3785.

26 P. Jiang, Y. Yang, R. Shi, G. Xia, J. Chen, J. Su, Q. Chen, *J. Mater. Chem. A*, 2017, **5**, 5475.

27 G. Chen, W. Chen, R. Lu, C. Ma, Z. Zhang, Z. Huang, J. Weng, Z. Wang, Y. Han, W. Huang, *J. Am. Chem. Soc*., 2023, **145**, 22069.

28 Y. Zhang, K. E. Arpino, Q. Yang, N. Kikugawa, D. A. Sokolov, C. W. Hicks, J. Liu, C. Felser, G. Li, *Nat. Commun*., 2022, **13**, 7784.

29 W. Li, L. Zhang, L. Ma, J. Wang, R. Qi, Y. Pang, M. Xu, C. Zhao, C. Wang, M. Gao, X. Lu, *Nano Lett*., 2024, **25**, 443.

30 Y. Luo, L. Tang, U. Khan, Q. Yu, H.-M. Cheng, X. Zou, B. Liu, *Nat. Commun*., 2019, **10**, 269.

31 Y. Tong, D. Feng, P. Chen, *ACS Sustain. Chem. Eng*., 2021, **9**, 10601.

32 S. Parvin, A. Kumar, A. Ghosh, S. Bhattacharyya, *Chem. Sci*., 2020, **11**, 3893.

33 S. Sarwar, A. Nautiyal, J. Cook, Y. Yuan, J. Li, S. Uprety, R. Shahbazian-Yassar, R. Wang, M. Park, M. J. Bozack, X. Zhang, *Sci. China Mater*., 2020, **63**, 62.

34 L. Li, W. Zou, Q. Ye, Q. Li, Q. Feng, J. Wei, X. Xu, F. Wang, *J. Power Sources*, 2021, **516**, 230657.

35 L. Zhang, Z. Yan, X. Chen, M. Yu, F. Liu, F. Cheng, J. Chen, *Chem. Commun*., 2020, **56**, 2763.

36 M. Zulqarnain, A. Shah, M. A. Khan, F. Jan Iftikhar, J. Nisar, *Sci. Rep*., 2020, **10**, 6328.

37 L. Tang, R. Xu, J. Tan, Y. Luo, J. Zou, Z. Zhang, R. Zhang, Y. Zhao, J. Lin, X. Zou, B. Liu, H.-M. Cheng, *Adv. Funct. Mater*., 2021, **31**, 2006941.

38 R. Xu, J. Huang, L. Cao, L. Feng, Y. Feng, L. Kou, Q. Liu, D. Yang, L. Feng, *J. Electrochem. Soc*., 2020, **167**, 026508.

39 R. Liu, Z. Gong, J. Liu, J. Dong, J. Liao, H. Liu, H. Huang, J. Liu, M. Yan, K. Huang, H. Gong, J. Zhu, C. Cui, G. Ye, H. Fei, *Adv. Mater.*, 2021, **33**, 2103533.

40 Z. Zheng, L. Yu, M. Gao, X. Chen, W. Zhou, C. Ma, L. Wu, J. Zhu, X. Meng, J. Hu, Y. Tu, S. Wu, J. Mao, Z. Tian, D. Deng, *Nat. Commun.*, 2020, **11**, 3315.

41 C. Zhang, Y. Luo, J. Tan, Q. Yu, F. Yang, Z. Zhang, L. Yang, H.-M. Cheng, B. Liu, *Nat. Commun.*, 2020, **11**, 3724.

42 Z. Zhang, Y. Wang, X. Leng, V. H. Crespi, F. Kang, R. Lv, *ACS Appl. Energy Mater.*, 2018, **1**, 1268.